J. Fluid Mech. (1991), *vol.* 233, *pp.* 633–660
Printed in Great Britain

Observations of the dynamics and acoustics of travelling bubble cavitation

By S. L. CECCIO† AND C. E. BRENNEN
California Institute of Technology, Pasadena, CA 91125, USA

(Received 6 August 1990 and in revised form 6 June 1991)

Individual travelling cavitation bubbles generated on two axisymmetric headforms were detected using a surface electrode probe. The growth and collapse of the bubbles were studied photographically, and these observations are related to the pressure fields and viscous flow patterns associated with each headform. Measurements of the acoustic impulse generated by the bubble collapse are analysed and found to correlate with the maximum volume of the bubble for each headform. These results are compared to the observed bubble dynamics and numerical solutions of the Rayleigh–Plesset equation. Finally, the cavitation nuclei flux was measured and predicted cavitation event rates and bubble maximum size distributions are compared with the measurements of these quantities.

1. Introduction

Though the dynamics and acoustics of travelling bubble cavitation have been extensively studied both experimentally and theoretically, the behaviour of naturally occurring cavitation bubbles near surfaces has not been examined in great detail. It has been known for some time that cavitation bubbles generated near surfaces are usually not spherical (as often assumed in theory) but hemispherical caps (Knapp & Hollander 1948; Parkin 1952), and a cavitation bubble collapsing near a solid boundary may produce a microjet of fluid which has been speculated to cause surface cavitation damage (Benjamin & Ellis 1966; Plesset & Chapman 1970; Lauterborn & Bolle 1975; Kimoto 1987; Vogel, Lauterborn & Timm 1989; and, for a review, Blake & Gibson 1987). The complex shapes that travelling bubbles assume will clearly be influenced by macroscopic flow phenomena such as pressure gradients, boundary layers, separation, and turbulence. Researchers have attempted to study these effects by observing cavitation bubbles induced in a venturi (Kling & Hammitt 1972) or above a surface (Chahine, Courbiere & Garnaud 1979; van der Meulen 1989). Yet detailed, systematic studies of hydrodynamically produced cavitation bubbles are almost non-existent. The random nature of naturally occurring cavitation is the primary reason why investigators have focused on integral measurements in their study of cavitating flows, leaving the detailed behaviour of individual cavitation bubbles unexamined.

Analyses of cavitation noise have generally been based on the theoretical behaviour of single, spherical bubbles following the work of Fitzpatrick & Strasberg (1956). From this data base, researchers have synthesized the acoustic emission from cavitating flows with multiple events (Blake 1986). Many experiments have

---

† Present address: Department of Mechanical Engineering and Applied Mechanics, University of Michigan, Ann Arbor, MI 48109-2121, USA.

attempted to extract the actual behaviour of individual bubbles from the integral measurement of the noise produced by cavitation (Mellon 1956; Blake, Wolpert & Geib 1977; Hamilton 1981; Hamilton, Thompson & Billet 1982; Marboe, Billet & Thompson 1986). Although trends are seen in the measured spectra which may be related to theoretical predictions, the difficulty of obtaining free field acoustic spectra in the confines of most water tunnels has always made interpretation of experimental spectra problematic.

Researchers have also attempted to treat cavitation as a stochastic process. The spectral emission of a cavitating flow will depend not only on the noise produced by single bubbles but also on the cavitation rate and event statistics (Morozov 1969; Baiter 1986). Furthermore, cavitation noise scaling like that suggested by Blake *et al.* (1977) will be significantly influenced by changes in the cavitation event rate. As the number of cavitation events increases, bubble interactions will affect individual bubble volume histories and their acoustic emission (e.g. Morch 1982; Arakeri & Shanmuganathan 1985; d'Agostino, Brennen & Acosta 1988). Analyses of multiple bubble effects depend upon a knowledge of the nuclei distribution in the flow and the dynamics causing the nuclei to cavitate.

Yet the effect of nuclei number distribution on the total cavitation process is poorly understood, and this is due largely to the difficulty of accurately measuring this quantity. In fact, most cavitation studies neglect to include any measure of the nuclei number distribution. As we shall demonstrate, the number and size distribution of cavitation bubbles, and the resulting noise emission, can vary substantially over the course of an experiment, even at a nominally fixed operating point. Although the mean cavitation event rate may be approximately determined by the acoustic pulse rate (Marboe *et al.* 1986), cavitation bubble size distributions have only been determined in very rough form (Baiter 1974; Meyer, Billet & Holl 1989). Despite knowledge of the cavitation rate and bubble size distribution being essential, no simple method has yet been found to count and measure cavitation bubbles.

The above observations indicate a need to study the dynamics and acoustic emission of individual cavitation bubbles. A method of detecting and measuring cavitation bubbles was needed, and this paper presents data obtained through the use of a new electrical probe developed for this purpose. Using this new instrument experiments were performed to study individual cavitation events and their statistics in an attempt to address the above issues.

2. Experimental set-up

The experiments were conducted in the Caltech Low Turbulence Water Tunnel (LTWT); a full description of the facility is presented by Gates (1977). For all experiments, the test-section free-stream velocity was set and the tunnel static pressure lowered until the desired cavitation number was reached. The operating air content was generally 6–8 p.p.m., and the tunnel water was well filtered. The free-stream nuclei number distribution of the upstream fluid was measured using in-line holography. A detailed description of the holographic system is presented by Katz (1981).

Two axisymmetric headforms were used in the present experiments. The first was a Schiebe headform with an ultimate diameter of 5.08 cm. (Gates *et al.* 1979); the second, which has a modified ellipsoidal shape with a diameter of 5.59 cm, is known as the ITTC headform (Lindgren & Johnsson 1966). Surface pressure distributions

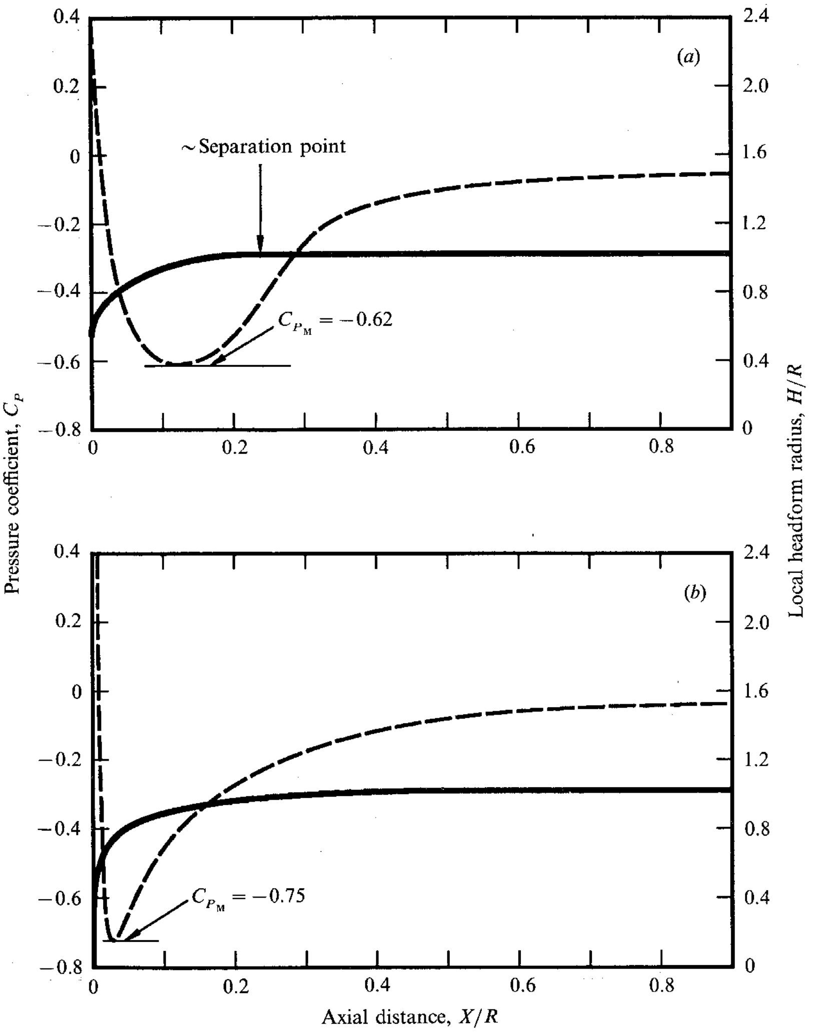

FIGURE 1. Surface pressure distributions and profiles of the (*a*) ITTC body and (*b*) the Schiebe body. H is the local radius of the body, X is the distance from the tip of the body along the axis, and R is the final radius of the body. C_P is the pressure coefficient.

for the Schiebe body (Gates *et al.* 1979) and the ITTC headform (Hoyt 1966) are available in the literature. The headform contours and surface pressure distributions are presented in figure 1, with the pressure coefficient, C_P, defined as $P_S - P_0/\frac{1}{2}\rho U_0^2$. P_0 and U_0 are the free-stream pressure and velocity and ρ is the density of water. P_S is the local surface pressure.

The headforms were fabricated out of lucite, a material whose acoustic impedance is a fair match to that of water. The hollow interior of both bodies was filled with water in which a hydrophone was placed. The hydrophone, an ITC-1042, has a relatively flat response up to 80 kHz. Except for ultra-low frequencies ($\ll 1$ Hz, the hydrophone signal was not filtered. All acoustic signals were digitized at a sampling rate of 1 MHz. Because of the relatively good acoustic impedance match between lucite and water, the interior hydrophone allows the noise generated by the cavitation bubbles to reach the hydrophone relatively undistorted; reflected acoustic signals from other parts of the water tunnel only make their appearance after the important initial signal has been recorded. The signal from the internal hydrophone was compared to that from an identical hydrophone positioned ≈ 10 hydrophone diameters away from the source of noise on the body. The two signals were similar and the magnitudes scaled with the acoustic path length.

In addition to the hydrophone, each headform was provided with novel equipment developed from instrumentation which had previously been used to measure volume fractions in multiphase flows (Bernier 1981). This instrumentation consisted of a series of electrodes arrayed on the headform surface which were used to detect and measure individual cavitation bubbles. A pattern of alternating electric potentials is applied to the electrodes and the electric current from each is monitored. When a bubble passes over one of the electrodes the impedance of the local conducting medium is altered, causing a change in the current from the electrode. This change, which is detected and recorded, permits the position and volume of the bubble to be monitored.

One specific electrode geometry consisted of patches arrayed in the flow direction to cover the major extent of the cavitating region. Another consisted of electrodes which encircled the entire circumference of the headform in the region of maximum bubble growth. These two electrode geometries were used for different purposes. Signals from the patch electrodes indicated cavitation at a specific location on the headform, and, by electronically triggering flash photography, simultaneous plan and profile photographs of individual bubbles could be taken at a prescribed moment in the bubble history. Thus, a whole series of bubbles could be inspected at the same point in their trajectory. Furthermore, by simultaneously recording the acoustic signal from the hydrophone, one could correlate the noise with the geometry of the bubbles.

The circular geometry was used to detect the occurence of every cavitation bubble at a particular location on the headform. This position was chosen to be near the location of maximum bubble volume, and for relatively moderate event rates only one bubble would occur over the electrode at any given time. Because almost all the cavitation bubbles maintain the same distance above the electrodes (this will be discussed below), the output of the circular elctrode system is directly proportional to the area covered by the bubble, and the peak of the signal is proportional to the major diameter of the bubble base. This system was calibrated photographically and found to be quite linear. The volume of the bubbles was then determined from a measure of the base diameter using a functional relationship derived through the photographic study of many individual bubbles (Ceccio 1990). Two kinds of experiments were performed with the circular electrode system. The first involved the measurement of event statistics and bubble maximum size distributions. In the second, the acoustic emission of individual cavitation bubbles was analysed and the result correlated with the bubble maximum volume.

Cavitation bubbles were observed on both the Schiebe and ITTC headforms over a range of cavitation numbers, σ, defined as $P_0 - P_V/\frac{1}{2}\rho U_0^2$, P_V is the water vapour pressure at the operating temperature. The cavitation number was varied between the travelling bubble cavitation inception value, σ_i, and the value at which attached cavitation occurred, σ_{ac}. The inception index on both bodies was strongly dependent on the ambient nuclei number distribution (Ooi 1981). Inception occurred on the Schiebe body at cavitation numbers as high as $\sigma_i = 0.65$, and on the ITTC body at $\sigma_i = 0.58$ for tunnel water of 6–7 p.p.m. air content. However, on both bodies the inception index was reduced to about $\sigma_i = 0.50$ immediately after deaeration. Any

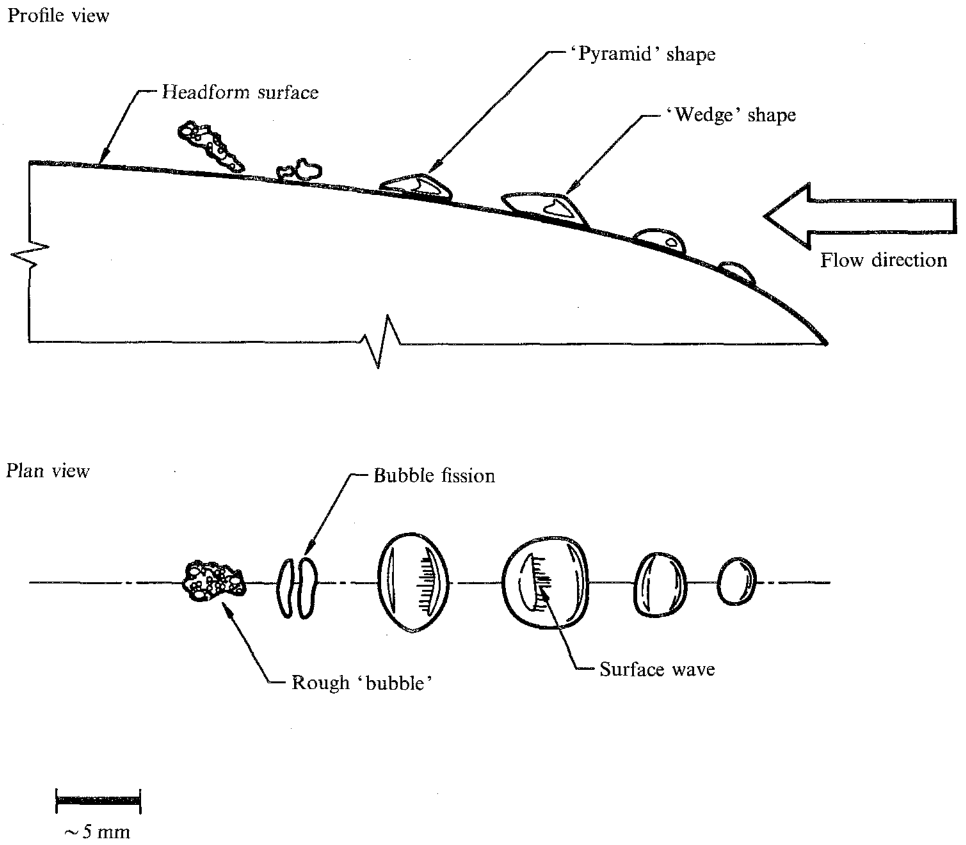

FIGURE 2. Schematic diagram of typical bubble evolution on the Schiebe headform.

definition of the bubble cavitation inception index must therefore be associated with a particular free-stream nuclei number distribution. The attached cavitation formation index for the Schiebe body was $\sigma_{\mathrm{ac}} = 0.40$ and for the ITTC body $\sigma_{\mathrm{ac}} = 0.41$. These values were almost constant over the fairly narrow range of Reynolds numbers of the experiments ($Re = 4.4 \times 10^5$–4.8×10^5, based on the headform final diameter).

Before detailing the results from each headform, one observation can be made for both geometries. For a given tunnel velocity and cavitation number, the maximum bubble volumes were quite uniform. Although the incoming nuclei diameter ranged over almost three orders of magnitude, the maximum cavitation bubble volume varied over only one order of magnitude. The reason for this is given below.

For both headforms, the growth phase of the nuclei was very similar to that described in the original observations of Knapp & Hollander (1948) and Ellis (1952). For most of their evolution, the bubbles take on a hemispherical or 'cap' shape and move extremely close to the headform surface; only very occasionally would quasi-spherical bubbles be observed at a distance above the surface. Small waves could be observed on the bubble surface in many instances. As the bubbles reach their maximum volume they become somewhat elongated in the direction normal to their motion while their thickness normal to the surface remains relatively constant. At this point, the difference in the flows around the two bodies begins to cause differences in the bubble dynamics.

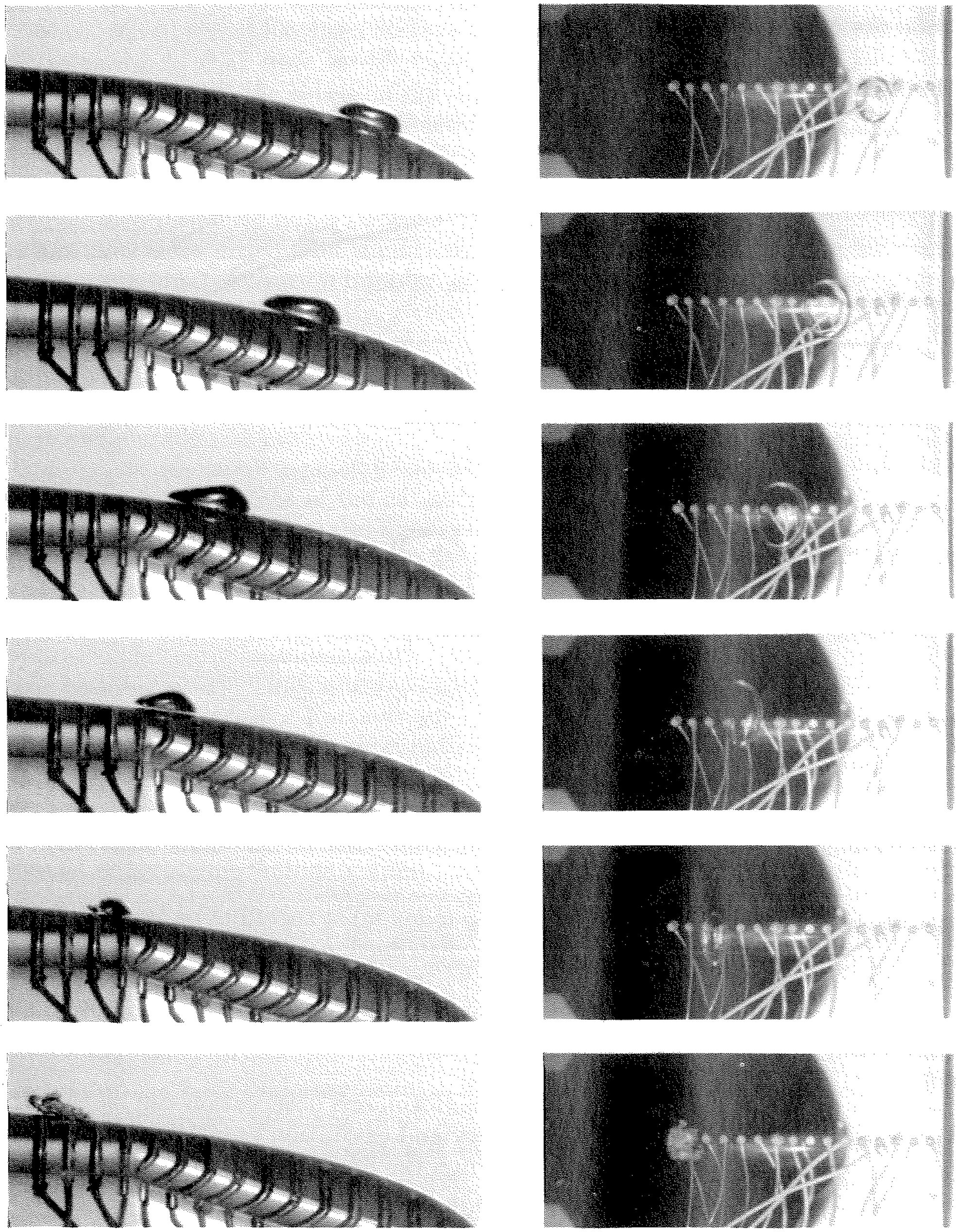

FIGURE 3. Series of photographs detailing typical bubble evolution on the Schiebe headform, $U = 9$ m/s and $\sigma = 0.45$.

The Schiebe body was designed to suppress laminar separation in the region of cavitation (Schiebe 1972), It possesses a sharp pressure drop with a minimum pressure coefficient of -0.75 (figure 1). Figure 2 represents a schematic of the typical bubble evolution, and figure 3 consists of a series of photographs of bubbles at various stages during this process. After the bubble has reached its maximum volume, it begins to lose its cap-like shape and becomes elongated, progressing into a pyramid-like shape; the bubble thickness normal to the headform surface

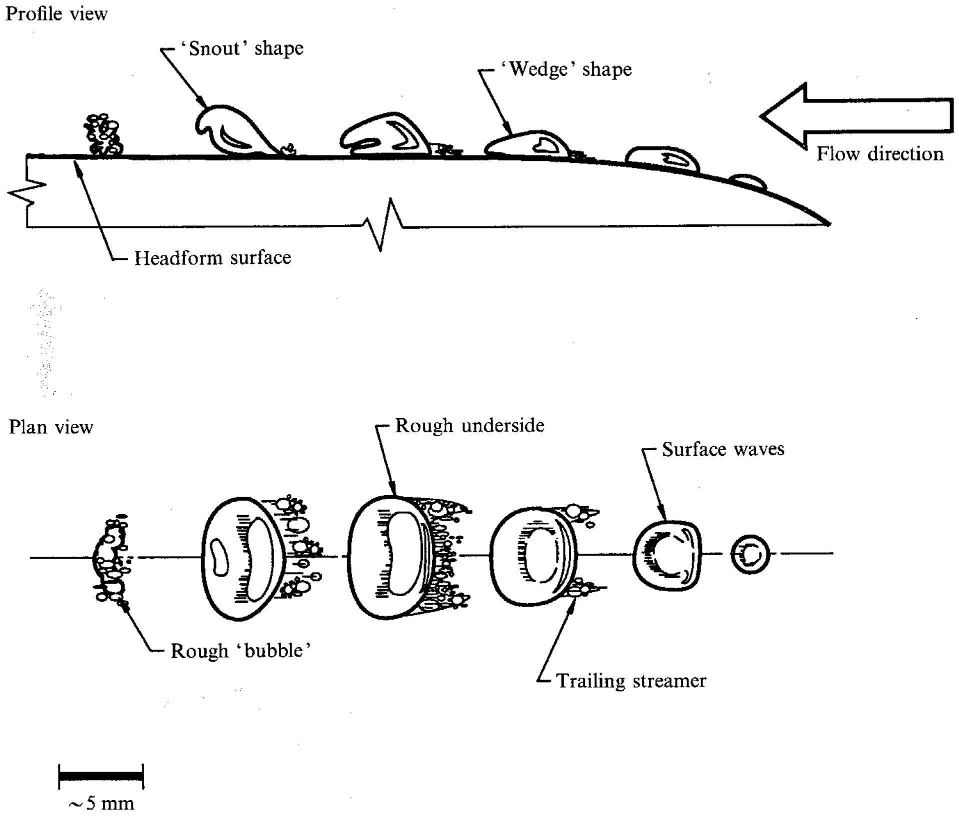

FIGURE 4. Schematic diagram of typical bubble evolution on the ITTC headform.

consistently decreases after reaching its maximum. The bubble then collapses rapidly and develops an elongated shape. The elongation of the bubble and the formation of tubes is probably due to rotation of the bubbles caused by the shear in the boundary layer. As the bubble collapses it may fission into two or three tubes of collapsing vapour, and the residual gas in these tubes may cause a rebound to produce a rough bubble or group of bubbles after collapse.

The ITTC headform has a relatively smooth pressure drop with a minimum pressure coefficient of -0.62. A distinguishing feature of this headform is that, unlike the Schiebe body, it possesses a laminar separation region (figure 1). Figure 4 is a schematic of the typical bubble evolution, and figure 5 presents a series of photographs of bubbles at various stages of this development. The bubble has a cap-like shape until it reaches its maximum volume where it then becomes further elongated evolving into the wedge-like shape. However, unlike the bubbles on the Schiebe body, the cavity starts to lift off the surface and begins to roll up into a snout-like shape. This may be due to recirculating flow associated with the separation region or the stretching of the bubble in the velocity gradient. As it collapses, the 'snout' continues to roll up into a vapour tube, eventually collapsing to produce a rough bubble after collapse.

On both the Schiebe and ITTC headforms, the rough bubble or group of bubbles which is formed after collapse is sheared by the surface flow and usually disperses into smaller bubbles on the order of 50 μm, although a second collapse and rebound is not uncommon. The mean lifetime of a bubble depends upon the tunnel velocity,

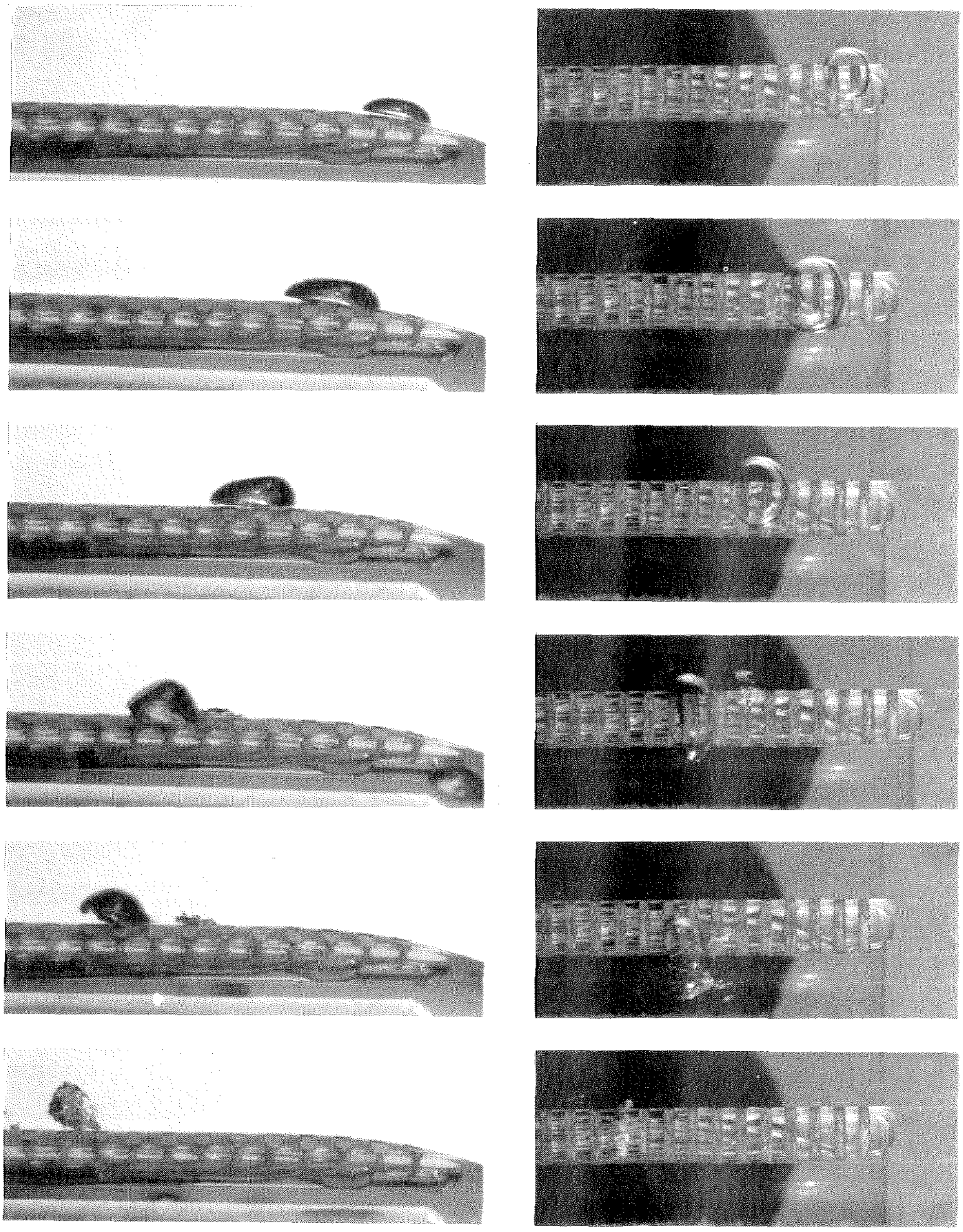

FIGURE 5. Series of photographs detailing typical bubble evolution on the ITTC headform, $U = 8.7$ m/s and $\sigma = 0.45$.

cavitation number, and initial nucleus size, but, for most of the observed bubbles on both headforms, it is approximately 3 ms.

The laminar separation on the ITTC body has been carefully studied in the context of its effect on attached cavitation (Arakeri & Acosta 1973). Clearly, the separated flow also influences bubble cavitation for cavitation bubbles were observed riding over the separation 'bubble'. As seen in figures 4 and 5, the underside of the bubbles becomes roughened as they pass over the region of turbulent reattachment. These

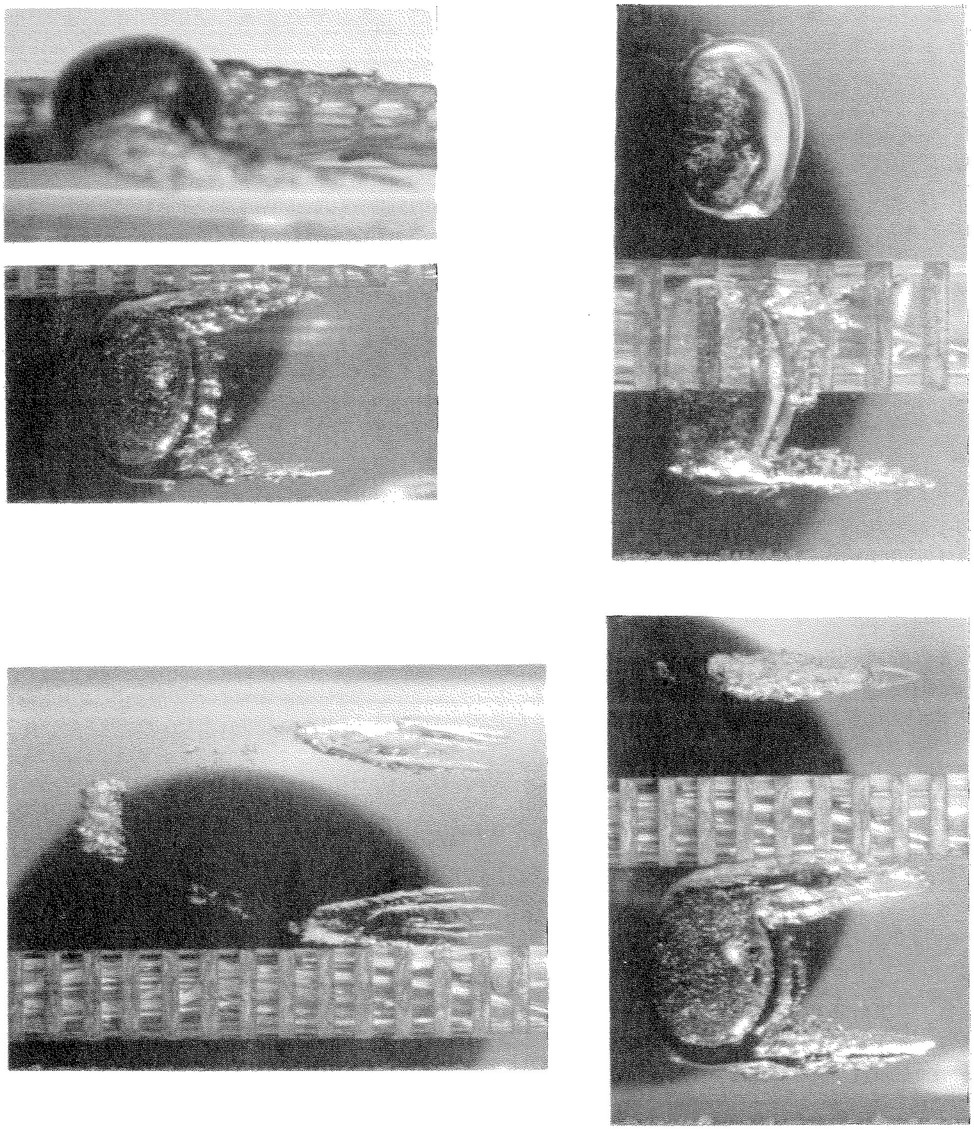

FIGURE 6. Series of photographs detailing bubbles with tails on the ITTC headform, $U = 9$ m/s and $\sigma = 0.42$.

local flow disturbances seem to shear vapour off the underside of the bubble, leaving a trail of much smaller bubbles. This phenomenon was not observed on the Schiebe body.

Furthermore, some bubbles were seen to cause local attached cavitation when the operating cavitation number was close to the attached cavity formation index. The attached cavitation appeared in the form of 'trailing streamers' left behind a moving bubble (figure 6). These streamers were generally associated with the larger bubbles on the ITTC body (and occasionally on the Schiebe body) and were seen to develop gradually at the location of the laminar separation point (Arakeri & Acosta 1973). As the bubble is swept downstream, the streamers continue to grow, and in many cases persist even after the bubble has collapsed. Why these bubbles cause the attached

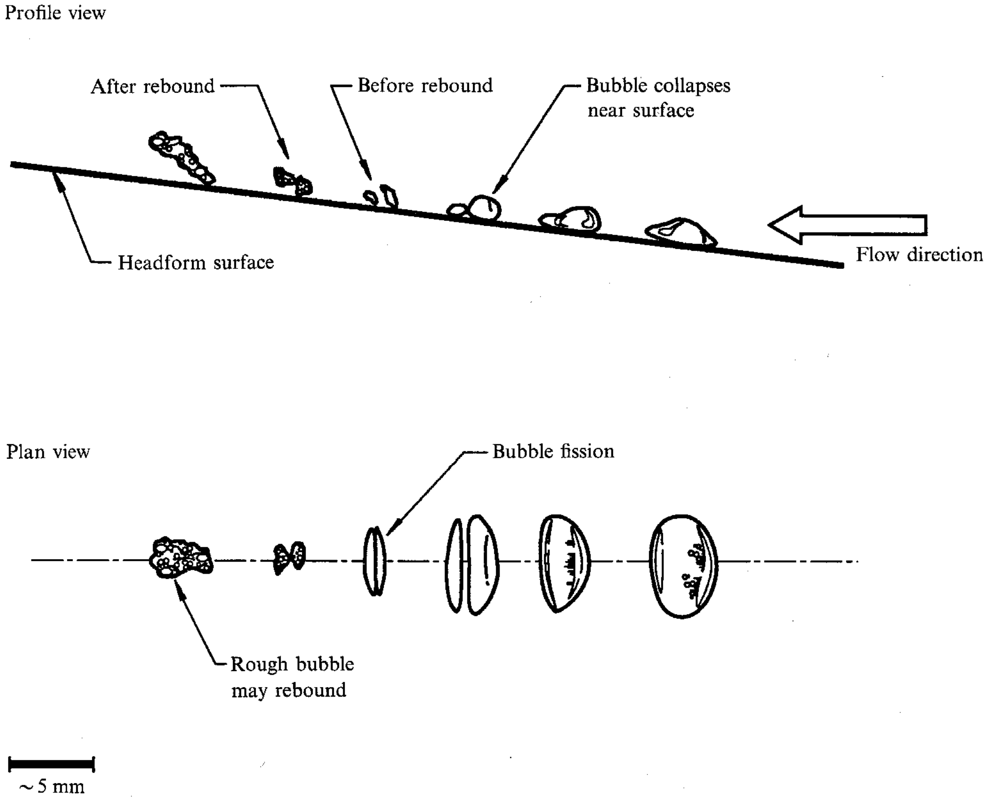

FIGURE 7. Schematic diagram of typical bubble collapse mechanism on the Schiebe headform.

cavitation streamers at the lateral extremities of the bubble is unclear. This phenomenon has also been observed with travelling bubble cavitation on hydrofoils (van der Meulen 1980; Rood 1989). The process could be considered an inception mechanism for attached cavities.

The classic observations of Knapp & Hollander (1948) may be compared with those of this study. Both experiments revealed that bubbles travelling near surfaces are cap shaped, and the gross characteristics of growth and collapse are similar. However, the pressure distribution on the ogive of Knapp & Hollander generated a long and steady growth, and the bubbles often retained a quasi-spherical shape even near the final stages of collapse. These bubbles would often rebound many times, maintaining their quasi-spherical shape after each collapse. The bubbles observed in this study usually rebounded only once and lost most of their coherent shape after the first collapse. This difference may be explained by noting that the water tunnel facility used by Knapp & Hollander was not equipped with any deaeration system, and extremely bubbly flows were used to increase the odds of photographing a cavitation event. Consequently, the cavitating nuclei observed by Knapp & Hollander were large, containing more undissolved gas. Increasing the amount of residual gas reduces the violence of the bubble collapse making coherent rebounds possible. On the other hand, the nuclei populations of the present study were quite small, and the cavitation bubbles observed were almost entirely vaporous. Such bubbles collapse violently and therefore coherent rebounds are less likely.

Photographs of bubbles presented by Ellis (1952) show many of the features in the

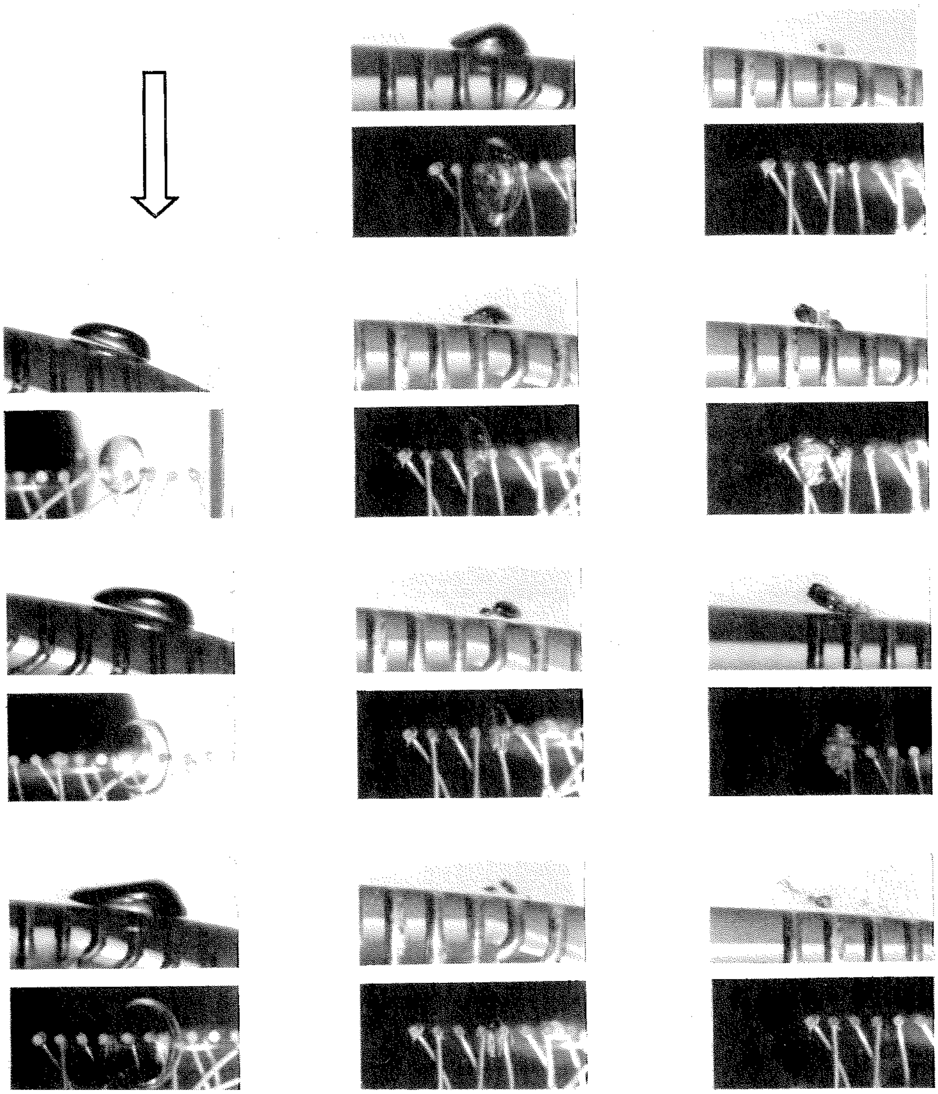

FIGURE 8. Series of photographs detailing typical bubble collapse mechanism on the Schiebe headform, $U = 9$ m/s and $\sigma = 0.45$.

present study. Principally, bubbles formed close to the headform also progressed from a cap shape to a wedge shape before collapse, although the collapse mechanism is difficult to distinguish in Ellis' silhouette images. He observed that the bubble surface profile approximately coincided with lines of constant pressure for bubbles near the point of maximum volume. This accounts for the wedge shape of the bubble. Examination of the isobaric lines computed for flow around the Schiebe body (Schiebe 1972) also show that the bubbles observed in this study are being shaped by the pressure gradients close to the surface.

Returning to the present study, the collapse mechanisms for bubbles on both headforms were discerned through the study of many photographs. A composite mechanism is presented in figure 7 for the Schiebe body with sample photographs in figure 8. Corresponding results for the ITTC body are included in figures 9 and 10.

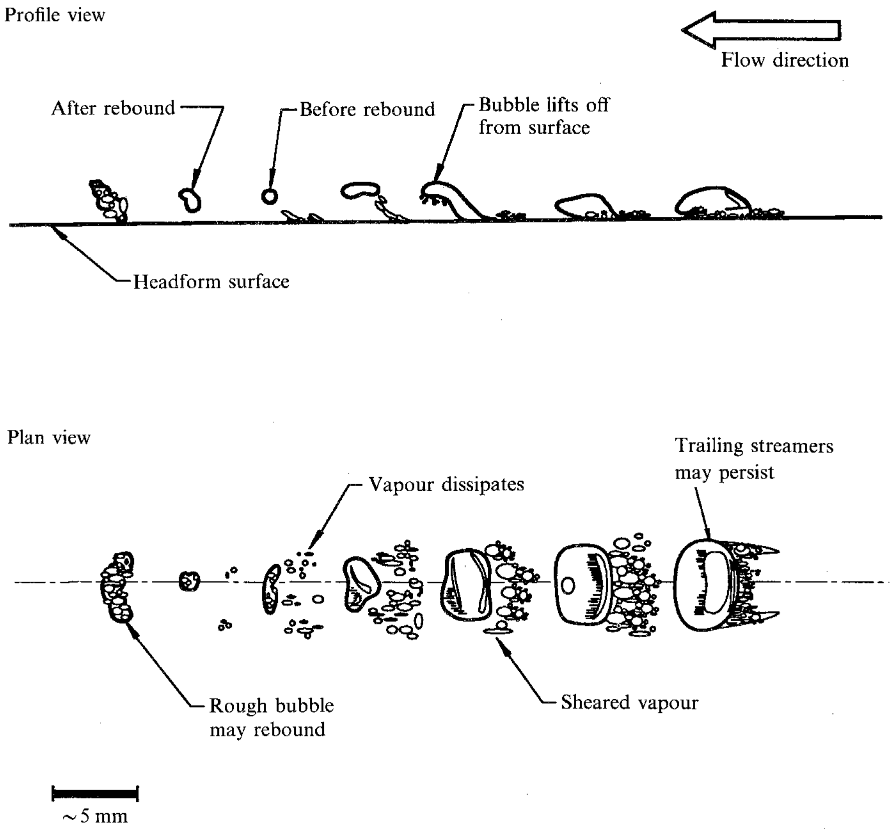

FIGURE 9. Schematic diagram of typical bubble collapse mechanism on the ITTC headform.

Previous researchers have noted the generation of a liquid microjet in bubbles collapsing near a solid surface (Lauterborn & Bolle 1975; Vogel *et al.* 1989; Kimoto 1987, for example), and this microjet is often surmised as the main cause of cavitation erosion damage. Although many photographs were taken during the present investigation; a re-entrant microjet was not observed in any of the present photographs of bubble collapse, although the jet may have occurred too rapidly to be detected. The observed bubbles lack the compact geometry we might expect to be associated with coherent microjet formation.

4. Measurement of the acoustic emission of single cavitation bubbles

The detailed relationship between the collapse mechanism of hydrodynamic cavitation bubbles and the resulting noise generation is not completely clear, but some features are suggested by the present work. First, as other investigators have concluded (for example Harrison 1952 and Chahine *et al.* 1979), the majority of the noise is generated by the violence of the first collapse; the growth phase contributed no measurable noise signal. The rebound produces a rough bubble which may also collapse to produce a second noise pulse of lesser magnitude. However, noise was not necessarily generated by every bubble collapse. Smaller bubbles would often collapse without an acoustic pulse, and larger bubbles would sometimes produce a muted collapse.

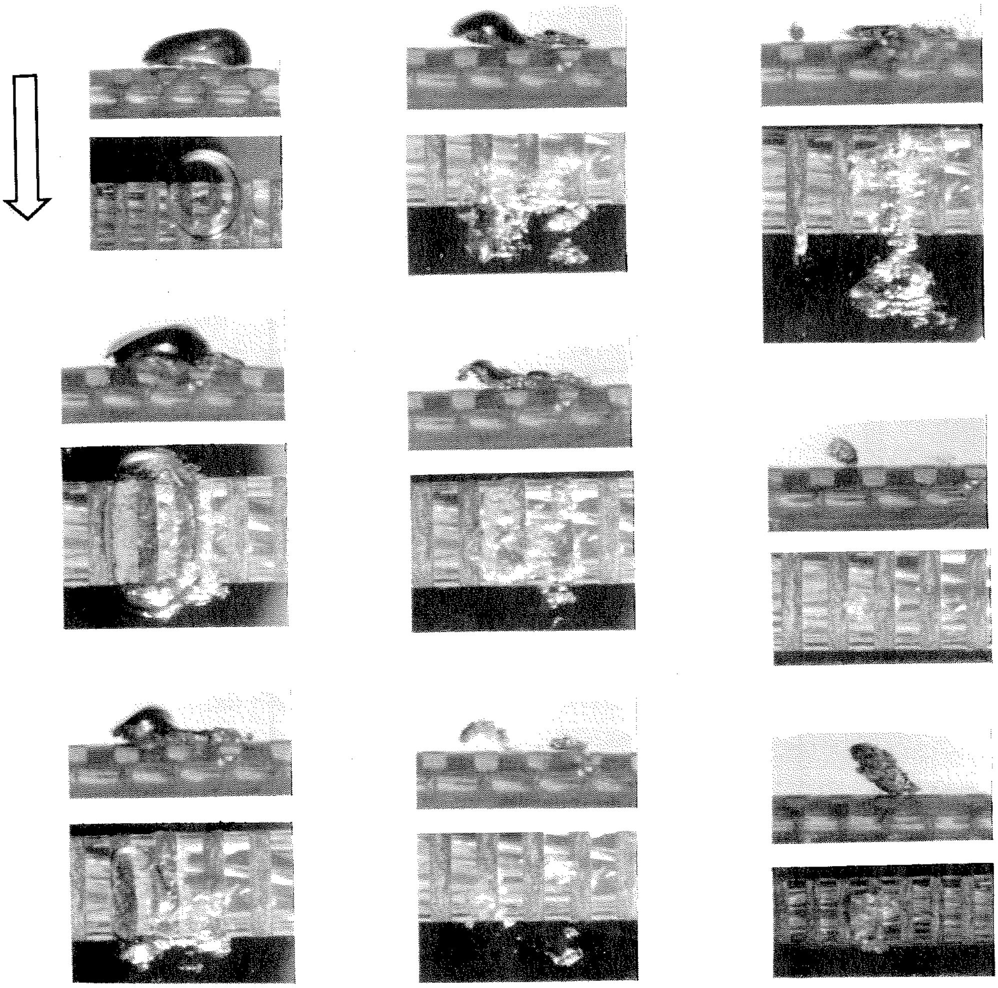

FIGURE 10. Series of photographs detailing typical bubble collapse mechanism on the ITTC headform, $U = 8.7$ m/s and $\sigma = 0.45$.

Figure 11 presents two examples of the initial noise pulse generated by the collapse of a bubble on the ITTC headform. The first pulse has only one peak, but the second trace is an example of a multiple peak event. Multiple peaks suggest bubble fission prior to collapse, and the photographs presented in the previous section reveal that many bubbles have undergone fission.

Although some researchers have used the peak acoustic pressure to characterize cavitation noise intensity (e.g. van der Meulen & Renesse 1989), in this study the magnitude of acoustic pulses will be characterized by the acoustic impulse defined as

$$I = \int_{t_1}^{t_2} P_A \, dt, \tag{1}$$

where P_A is the pressure pulse generated by the collapsing bubble. The times t_1 and t_2 were chosen to exclude the shallow pressure rise before collapse and the reverberation produced after the collapse (as shown in figure 11). Experimentally measured impulses for the Schiebe body at a tunnel velocity of $U = 9$ m/s and

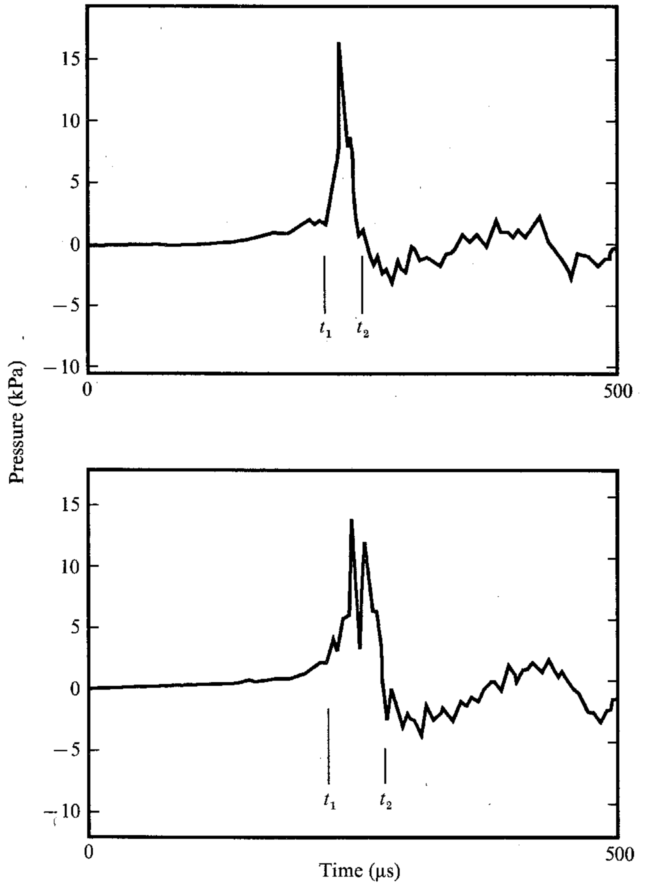

FIGURE 11. Two examples of typical cavitation initial noise pulses. The bubbles were generated on the ITTC headform at $\sigma = 0.45$ and $U = 8.7$ m/s.

cavitation numbers of $\sigma = 0.55$ and 0.42 are presented in figures 12 and 13. All the data appear to lie below an envelope which passes through the origin. The existence of this well-defined impulse envelope suggests that a collapsing bubble can generate, for a certain maximum volume, a specific impulse if it collapses in some particular but unknown way. It can, however, produce less than this maximum impulse if it collapses in other ways.

The different symbols represent the different number of acoustic peaks which are generated upon collapse. Note that '+' signifies an event with zero peaks, or, in other words, a mute collapse. As shown in figure 12, the probability that a collapse will produce multiple peaks increases for larger bubbles. Yet, even as the number of peaks increases, the impulse often reaches its maximum possible value implying that, in some collapse mechanisms, fission does not decrease the total stored energy available to produce noise. Other large bubbles collapse to produce almost no acoustic impulse. The production of noise upon collapse is the result of violent changes in bubble volume near the point of minimum bubble volume, but larger bubbles may be sheared apart and dissipate, thus losing their organized shape and preventing a coherent and concentrated collapse. Furthermore, larger bubbles may contain more contaminant gas (as a result of dissolution) and this would cushion the collapse and reduce the acoustic emission.

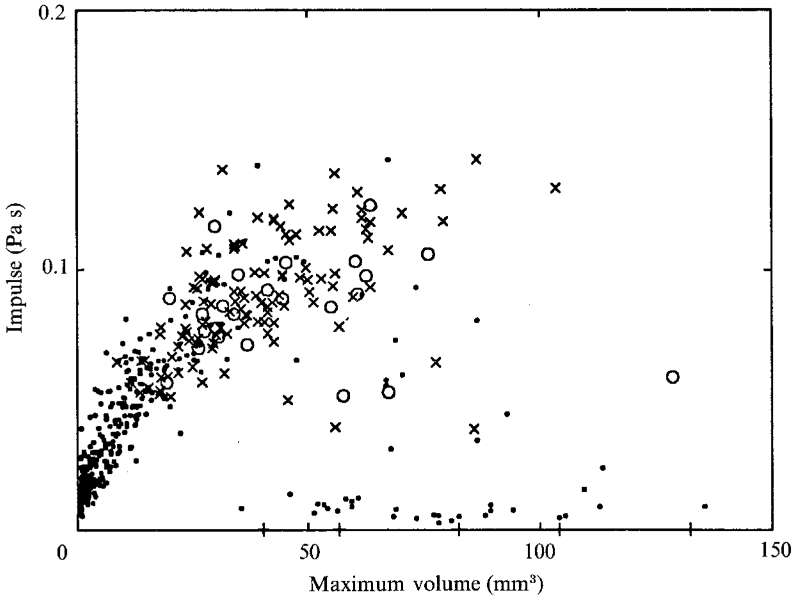

FIGURE 12. Acoustic impulse plotted against the maximum bubble volume for the Schiebe body at $U = 9$ m/s and $\sigma = 0.42$: +, represents an event with no measured impulse; ●, an event with one acoustic peak; ×, an event with two peaks; ○, an event with more than two peaks.

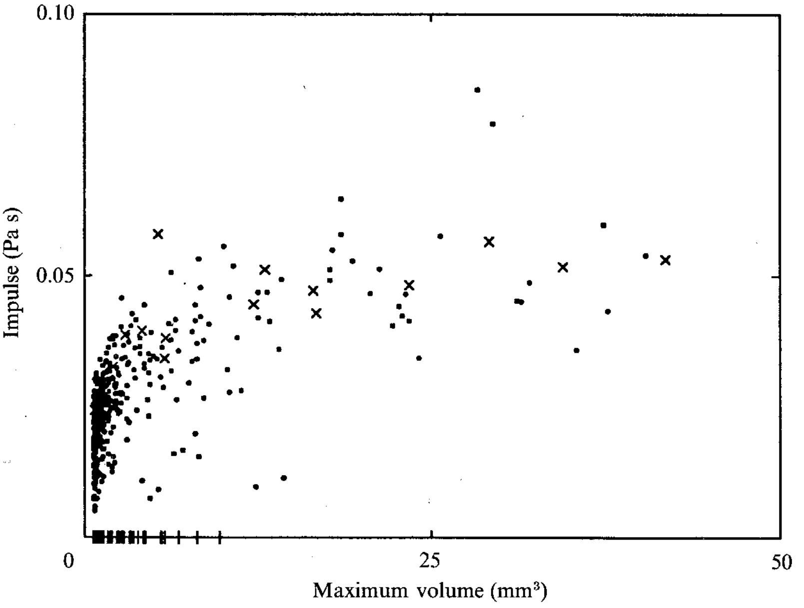

FIGURE 13. As figure 12 but at $\sigma = 0.55$.

At higher cavitation numbers such as that of figure 13 the number of larger bubbles is reduced, and most bubbles collapse to produce only one acoustic pulse. However, a large number of very small bubbles will collapse and produce no significant impulse. Mute events are generally not examples of 'pseudo-cavitation' as observed by Dreyer (1987) but distinct cavitation events with a near-silent collapse mechanism.

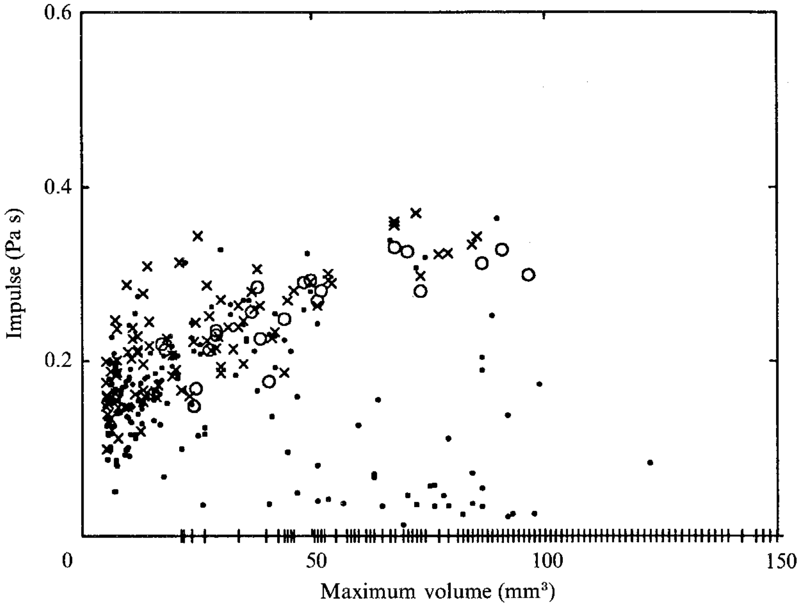

FIGURE 14. As figure 12 but for the ITTC body at $U = 8.7$ m/s and $\sigma = 0.42$.

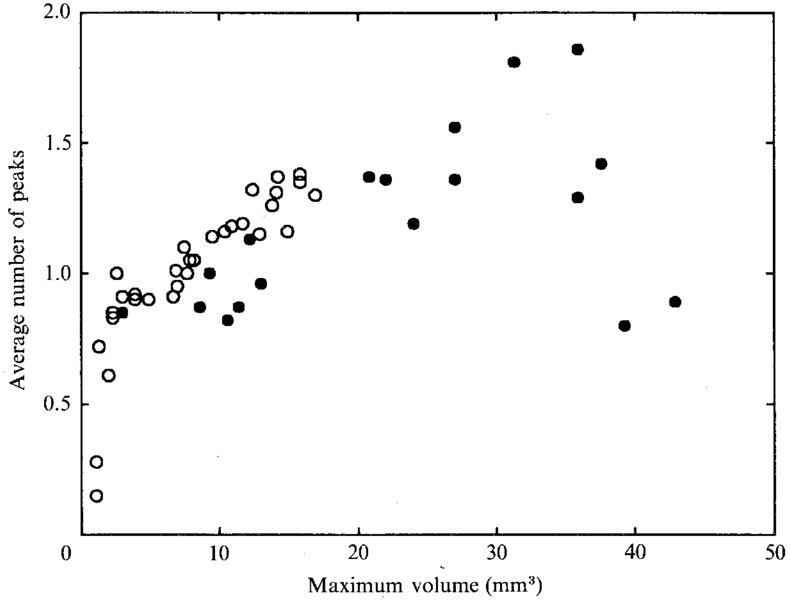

FIGURE 15. Average number of peaks as a function of average maximum bubble volume for bubbles generated on the Schiebe body (open symbols) and the ITTC body (closed symbols).

The general trends in the data for the Schiebe body are also evident in the results from the ITTC headform. Significantly, however, the average acoustic impulse is about three times larger than that of the Schiebe body. This will be discussed further below. Furthermore, as the cavitation number is lowered to near the attached cavitation inception index of the ITTC body, the impulse data change significantly. Figure 14 presents an example of data from the ITTC body taken at a tunnel velocity of $U = 8.7$ m/s and a cavitation number of $\sigma = 0.42$, near the attached cavitation formation index. The impulses generated by smaller bubbles are much more uncertain, and, for many larger bubbles, no significant impulse is generated. Since these larger bubbles generally have trailing streamers, it would seem that the streamers interfere with the collapse in a way which decreases or eliminates the noise.

The average number of peaks for a given average diameter is plotted in figure 15 for both headforms. For smaller bubbles, the average is less than unity, reflecting the influence of muted bubbles, and for larger bubbles, multiple peaking produces an average above unity. For the case of the ITTC body, however, the muting effect of the trailing streamers causes a reduction in the average number of peaks for the data set with the largest average volume. This data set occurs at the lowest cavitation number, near the attached cavitation inception point.

5. Comparison with analytical results

In order to place the above experimental results in some rough analytical perspective, calculations were made of the bubble sizes and acoustic impulses predicted by integration of the Rayleigh–Plesset equation starting with various sizes of free-stream nuclei. The known surface pressure distributions for both headforms were employed to construct the pressure–time history which a nucleus would experience while passing near the headform as it grew into a spherical bubble. No slip between the bubble and the liquid and a small offset from the stagnation streamline are assumed. Calculations were performed with various free-stream velocities, cavitation numbers, and offsets from the stagnation streamline. Figure 16 provides an example of the dependence of the maximum bubble radius, R_{M}, on the original nucleus size, R_0, for the ITTC headform and various cavitation numbers. Note that nuclei below a certain size (which depends on the cavitation number) hardly grow at all and would therefore not contribute visible cavitation bubbles. This critical size is predicted by the stability analysis of Johnson & Hsieh (1966) and Flynn (1964). Bubbles below the critical size grow quasi-statically, whereas larger bubbles grow explosively. A bubble is critically unstable if

$$\frac{R_{\mathrm{L}}}{R_{\mathrm{H}}} > \frac{8}{3}\frac{S}{\rho R_{\mathrm{H}} U^2}\frac{1}{(-\sigma - C_{P\mathrm{M}})}, \tag{2}$$

where $C_{P\mathrm{M}}$ is the minimum pressure coefficient, R_{H} is the headform radius, and R_{L} is the local bubble size as it travels near the headform. The computations show that a nucleus of initial radius R_0 will remain stable if R_{L} remains in the range $R_0 < R_{\mathrm{L}} < 2R_0$ for the common circumstances of interest here. Consequently, the critical nucleus size R_{C} is given by

$$R_{\mathrm{C}} > \frac{8}{3}\frac{\beta S}{\rho U^2}\frac{1}{(-\sigma - C_{P\mathrm{M}})}, \tag{3}$$

where β is a constant. The results of this simple expression are presented in figure 17 for two Weber numbers, $We = S/\rho_{\mathrm{L}} R_{\mathrm{H}} U^2$, along with data on the critical nucleus size obtained from the Rayleigh–Plesset solutions. The qualitative agreement is excellent and suggests a value of β slightly greater than 0.5. Note that the higher the velocity, U, the smaller the critical size, and therefore the larger the number of nuclei that will be involved in cavitation.

The other feature of figure 16 which is important to note is that virtually all nuclei greater than the critical nucleus size grow to approximately the same maximum size. The asymptotic growth rate of an unstable cavitating bubble is a function only of the pressure and not the initial nucleus size. Consequently, the maximum size achieved will be approximately independent of the nucleus size. This accounts for the near

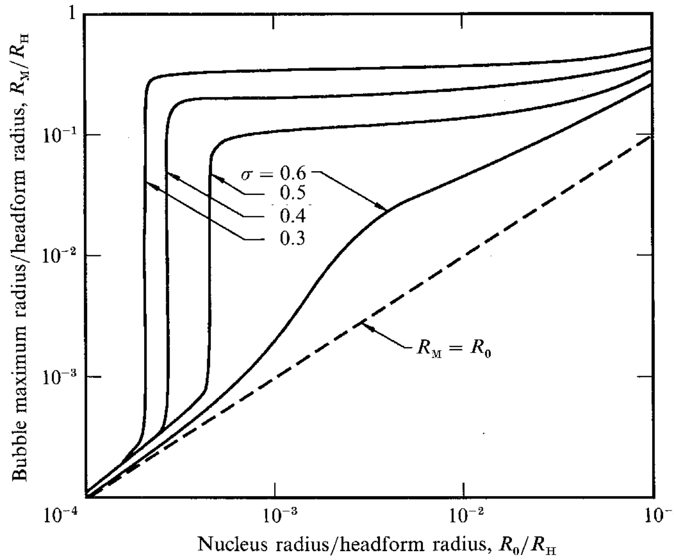

FIGURE 16. Numerical calculation of the bubble maximum radius as a function of nucleus radius for nuclei passing near the ITTC headform.

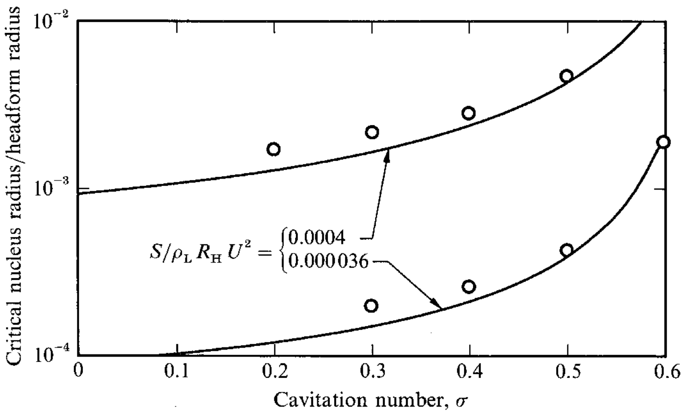

FIGURE 17. Critical nucleus radius as a function of the cavitation number and two Weber numbers for nuclei passing near the ITTC headform.

uniformity of cavitation bubbles observed experimentally. Similar calculations were performed for nuclei experiencing the Schiebe body pressure distribution, and the results were qualitatively similar to those of the ITTC body. The small effect that nuclei size has upon the maximum bubble size will be discussed in §6.

The above calculations yield the volume–time history for a cavitating bubble, and the acoustic pressure generated by the bubble may be approximately given by

$$P_A(r,t) = \frac{\rho}{4\pi r}\frac{d^2V}{dt^2}, \tag{4}$$

where $V(t)$ is the bubble volume, ρ is the fluid density, and r is the distance from the centre of the bubble. This relationship is valid in the acoustic far field and for subsonic wall velocities. The acoustic impulses, I, were calculated from the definition (1), where t_1 and t_2 were taken to be the times when $d^2V/dt^2 = 0$ before and after the first collapse.

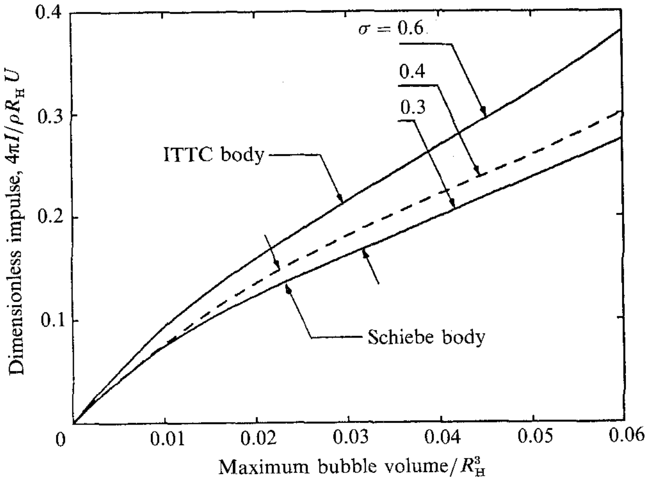

FIGURE 18. Numerical calculation of the acoustic impulse as a function of the maximum bubble volume for bubbles generated on the Schiebe body and the ITTC body for a range of cavitation numbers and two Weber numbers. Data for $0.3 < \sigma < 0.6$ and $We = 0.0004$ and 0.000036 for the ITTC body lie within the envelope shown. Data for $0.3 < \sigma < 0.4$ and $We = 0.0004$ and 0.000036 for the Schiebe body lie within the envelope shown.

A non-dimensional impulse, I^*, is defined as

$$I^* = \frac{4\pi I}{\rho R_H U}, \tag{5}$$

where we have assumed $r = R_H$ since this is the location of the hydrophone in the experiments. The impulse I^* is plotted in figure 18 against the maximum volume of the bubbles non-dimensionalized by R_H^3. A number of investigators (i.e. Fitzpatrick & Strasberg 1956; Hamilton *et al.* 1982) have suggested that the magnitude of the acoustic signal should be related to the maximum size of the bubble, and this is born out in figure 18 where the data for a range of cavitation numbers and two Weber numbers are contained within a fairly narrow envelope.

The median line was converted to dimensional values and is plotted in figure 19 where it is compared with averaged data sets from the Schiebe and ITTC experiments. It is striking to note that the envelope of the maximum impulse from the experiments is within a factor of two of the Rayleigh–Plesset calculation for the ITTC body and within a factor of six for the Schiebe body. This suggests that, despite the departure from the spherical shape during collapse, the incompressible Rayleigh–Plesset solutions correctly predict the order of magnitude of the noise impulse generated by individual bubbles.

It is not surprising that the predicted impulse is greater than the experimental value. In fact, the theoretical impulse may be considered the maximum impulse possible for a given bubble volume since a spherically symmetric collapse is probably the most efficient noise producing mechanism. The difference between the measured impulses and the theoretical impulse is an indication of the inefficiency of the actual collapse mechanism. Furthermore, the average impulses are closer to the theoretically predicted values for the ITTC body than for Schiebe body, and this is consistent with the photographic evidence that the ITTC collapse mechanism is more compact than that on the Schiebe body.

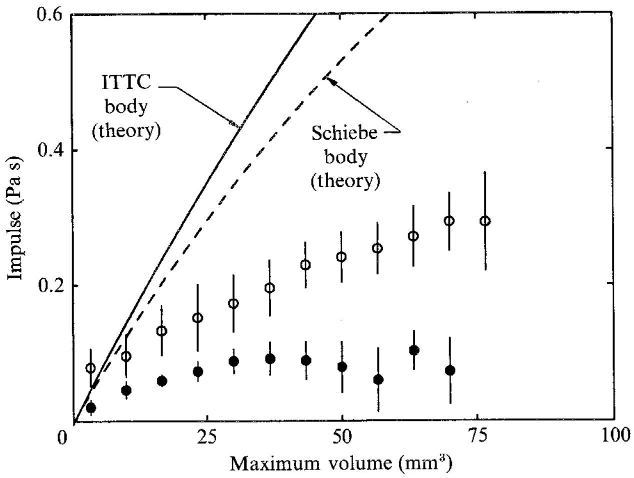

FIGURE 19. Comparison of theoretically predicted and experimentally measured acoustic impulse as a function of the maximum bubble volume or bubbles generated on the Schiebe body (open symbols) and ITTC body (closed symbols). Experimental data for $\sigma = 0.45$ and $U = 9$ m/s for the Schiebe body and $U = 8.7$ m/s for the ITTC body.

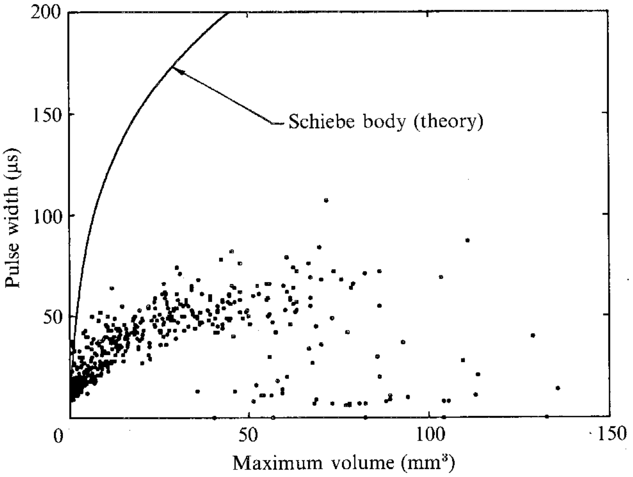

FIGURE 20. Comparison of theoretically predicted and experimentally measured pulse width as a function of the maximum bubble volume for bubbles on the Schiebe body at $U = 9$ m/s and $\sigma = 0.42$.

The duration of the impulse (as opposed to the magnitude) is much better understood. Here, the duration is defined as $T = t_1 - t_2$. This time is simply related to the total collapse time derived by Rayleigh (1917) which is used by many authors (e.g. Blake *et al.* 1977; Arakeri & Shanmuganathan 1985). Like the collapse time, it will be approximated by

$$T^* = \alpha \frac{R_M}{U_0} \left(\frac{2}{\sigma}\right)^{\frac{1}{2}}, \tag{6}$$

where α is some constant of order unity. It follows that the dimensionless impulse duration $T^* = TU_0/R_H$ should be primarily a function of R_M/R_H, and this is confirmed by the results of the Rayleigh–Plesset solutions shown in figure 20. Also plotted are typical experimental data from the Schiebe body, which are approxi-

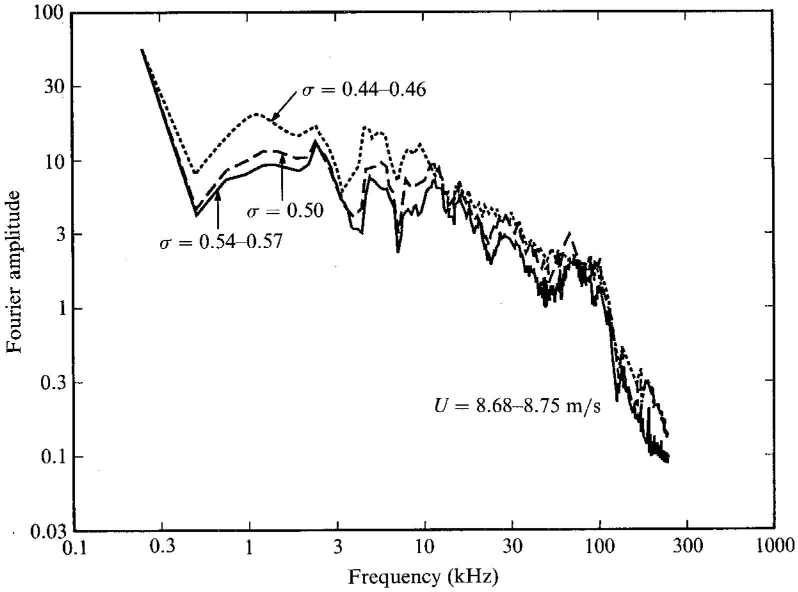

FIGURE 21. Averaged acoustic spectra derived from acoustic pulses generated by bubbles on the Schiebe body at average $U = 8.7$ m/s and $\sigma = 0.45$, 0.50, and 0.56 m/s. The vertical scale is arbitrary.

mately one third the predicted magnitude. It should be noted, however, that the definitions of t_1 and t_2 are somewhat arbitrary, and while this does not significantly affect the measurement of the acoustic impulse, it does add some uncertainty to the pulse width measurement. Also, the finite slew rate of the hydrophone will modify the measurement of the pulse width.

Figure 21 presents spectra of the noise measured in the experiments. A series of individual acoustic pulses were recorded at a particular velocity and cavitation number. The resulting spectra were averaged to produce the composite spectra in the figure; the signals were not altered to remove the effects of tunnel reverberation. Such a composite spectrum will be equivalent to the spectrum derived from a measurement of a long series of cavitation noise pulses, provided the cavitation events occur randomly (Morozov 1969). The measured spectral shape varies little with cavitation number; only the overall spectral magnitude changes. A decrease of approximately −12 dB/decade is noted until about 100 kHz where a sharp falloff occurs. This cutoff frequency corresponds to the frequency response limit of the hydrophone.

Asymptotic analyses of the Rayleigh equation (Blake 1986) predict a spectral shape of $f^{-\frac{2}{5}}$ for frequencies in the range of 10 to 100 kHz. The experimental spectrum has a shape of approximately $f^{-\frac{3}{5}}$ which is similar but not identical to the predicted trend. Hamilton (1981), on the other hand, observed an almost completely flat spectrum in this range based on his integral measurement of bubble cavitation noise. The high-frequency roll-off associated with fluid compressibility was not observed below 100 kHz, and this is consistent with the observations of Hamilton (1981) and Barker (1975).

6. Observations of cavitation event rates and bubble maximum size distributions

Experiments were performed to measure the cavitation event rate and bubble maximum size distribution on both headforms along with the free-stream nuclei number distribution. Furthermore, an analytical model was derived to study the relationship between the nuclei flux and the resulting cavitation statistics.

The cavitation event rate and bubble maximum size distribution were measured for several thousand events at various operating conditions, and examples of these measurements for the Schiebe headform are given in figure 22. Note that the bubble maximum sizes are presented as reduced radii. The reduced bubble radius is the radius of a sphere of volume equal to the measured bubble volume. Although the four bubble size distributions presented are all at the same cavitation number and tunnel velocity, their event rates and size distributions are quite different. Since the cavitation bubble maximum volume distribution is directly related to the incoming nuclei number distribution these results clearly indicate that the nuclei number distribution can be quite different for the same tunnel operating conditions. Weak control of the number of nuclei was effected through deaeration and nuclei injection. But, as figure 22 indicates, the nuclei number distribution is a highly variable factor which influences travelling bubble cavitation and cavitation noise. The time between cavitation events was Poisson distributed, as would be expected for randomly distributed nuclei. Consequently, the shape of the total noise spectra produced by these flows should correspond to the composite spectra presented in figure 21.

A relationship between the nuclei flux and the resulting cavitation event rate and bubble maximum size distribution can be developed as follows. Whether a nucleus cavitates or not is strongly determined by the local minimum pressure it experiences. On the surface of the headform, this pressure is given by the minimum pressure coefficient. On streamlines above the body surface, the fluid pressure may still be low enough to cause a nucleus to cavitate provided that the minimum pressure it experiences is below the critical pressure, derived from equation (3). An incoming streamtube may therefore be defined for a nucleus of specific size such that the nucleus will always encounter a pressure low enough to cause it to cavitate during its flow around the body. The fluid capture area of this streamtube will be a function of the nucleus radius, R_0, the free-stream cavitation number, and the flow geometry. By assuming that the pressure gradient normal to the surface corresponds to the centrifugal pressure gradient caused by the radius of curvature, κ, of the surface at the minimum pressure point, and by assuming no slip between the nuclei and the fluid, the following expression for the nuclei capture area, $A(R_0)$, may be readily obtained (Ceccio 1990):

$$A(R_0) = \frac{R_{\mathrm{B}}\kappa\pi}{(1-C_{PM})^{\frac{1}{2}}}(-\sigma - C_{PM})\left(1-\frac{R_{\mathrm{C}}}{R_0}\right), \tag{7}$$

where R_0 is the original nuclei radius, R_{B} is the headform radius at the point of minimum pressure, and R_{C} is the minimum cavitatable nucleus given by equation (3). Equation (7) may be rewritten as

$$A(R_0) = A_{\mathrm{V}}\left(1-\frac{R_{\mathrm{C}}}{R_0}\right), \tag{8}$$

where A_{V} is the capture area enclosing all streamlines which involve pressures less

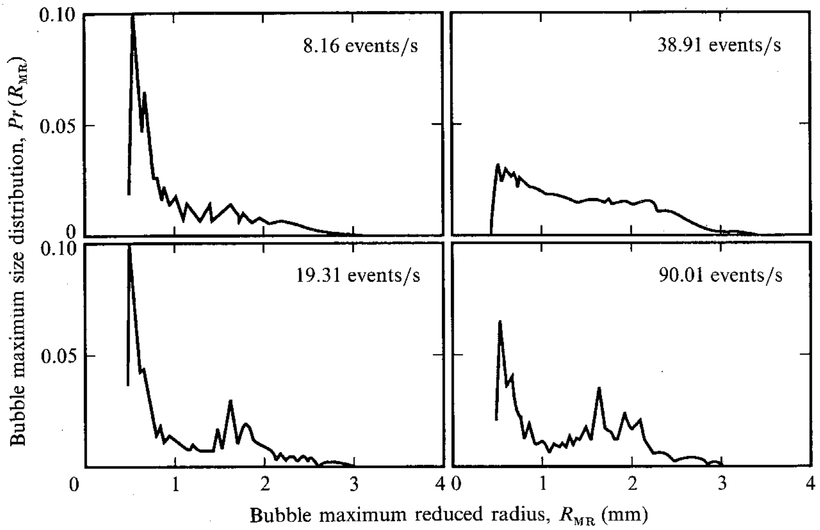

FIGURE 22. Examples of four bubble maximum size distributions for a particular free-stream velocity and cavitation number for cavitation on the Schiebe body.

than vapour pressure; not that A_V is a function only of the flow geometry and free-stream conditions. Finally, the total flux of cavitatable nuclei or total cavitation event rate, Θ, is

$$\Theta = \int_{R_C}^{\infty} A(R_0) N(R_0)\, U_0 \, \mathrm{d}R_0, \tag{9}$$

where $N(R_0)$ is the free-stream nuclei number distribution.

Now consider the distribution of bubble maximum sizes which this process will produce. This distribution is the result of different nuclei trajectories and sizes. Cavitating nuclei travelling on streamlines farther away from the headform will not grow to the same maximum volume as those travelling near the surface. Consequently, a flux of uniform nuclei, R_0, will yield a probability distribution of bubble maximum sizes, R_M, denoted by $Pr_0(R_M)$. Because of the slight dependence of bubble maximum size upon nucleus size, $Pr_0(R_M)$ is a function of R_0. A flux of nuclei represented by the nuclei number distribution, $N(R_0)$, will therefore produce a distribution of maximum bubble sizes, $Pr(R_M)$, given by

$$Pr(R_M) = \frac{1}{\Theta} \int_{R_C}^{\infty} Pr_0(R_M) A(R_0) N(R_0)\, U_0 \, \mathrm{d}R_0. \tag{10}$$

If no relationship existed between nucleus size and the maximum bubble size, $Pr(R_M)$ would be independent of the nuclei number distribution; changes in $N(R_0)$ would merely change the total event rate. The experimental data indicate, however, that the bubble maximum size distributions are influenced by the nuclei number distribution. The varying event rates reported in figure 22 indicate different nuclei populations, and each example is accompanied by a unique bubble size distribution. The small influence of nucleus size upon the maximum bubble size will ultimately have a significant influence upon the bubble maximum size distribution.

We shall now compare the measured cavitation event rates and bubble maximum size distributions with the predicted quantities based on holographically determined

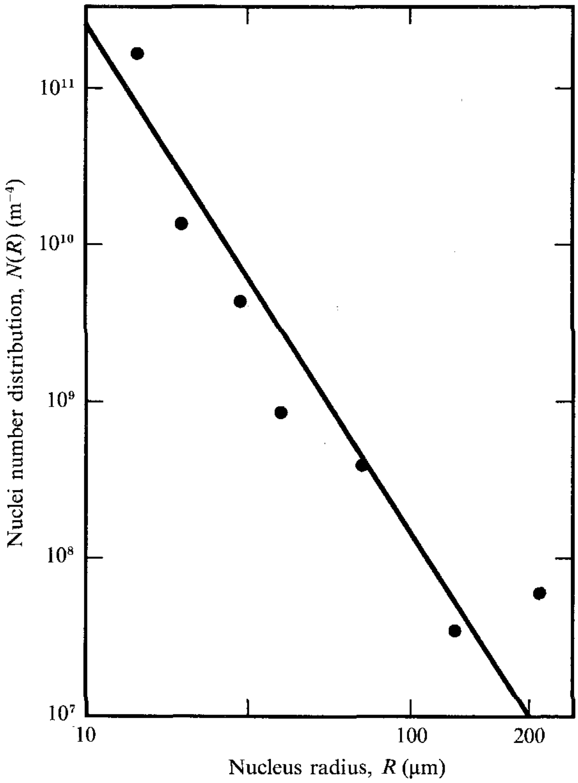

FIGURE 23. Example measurement of the free-stream nuclei number distribution, $U = 9$ m/s and σ0.45 (line is best fit to data points).

Predicted Θ (events/s)	Measured Θ (events/s)
128±25	156
164±25	147
147±25	162

TABLE 1. Comparison of measured and predicted cavitation event rates for cavitation generated on the ITTC body at $U = 9$ m/s and $\sigma = 0.45$.

free-stream nuclei distributions. The nuclei populations were measured at the same time that the cavitation statistics were recorded, and the smallest nucleus which could be detected with certainty was approximately 20 μm in diameter. An example nuclei distribution is presented in figure 23. Table 1 presents the measured event rates and the predicted event rates based on (7) and (9). The measured event rates fall within the range of the predicted values, with the uncertainty in the predicted event rates resulting from uncertainty in the measured nuclei number distributions. The close match between the predicted and measured event rates indicates that the nucleus stability criterion from (3) adequately models the actual cavitation process. The minimum cavitable nucleus for this flow is calculated to be approximately 20 μm in radius, and the measured nuclei number distributions indicate that most of

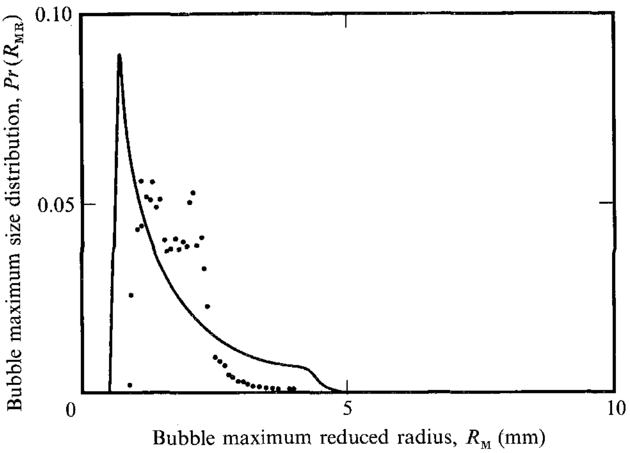

FIGURE 24. Calculated (——) and measured (data points) bubble size distribution for cavitation on the ITTC headform at $U = 9$ m/s and $\sigma = 0.45$. Calculated event rate = 128 events/s; measured event rate = 156 events/s.

the cavitating nuclei are in the range 20 to 100 μm. The success of the model suggests that the quantities A_V and R_C may be used to adequately characterize the nuclei capture area for flows over more complicated bodies.

The calculated bubble maximum volume distributions, however, depart substantially from the measured size distribution in its details. Figure 24 presents a measured bubble maximum size distribution along with the predicted distribution based on (7), (9), and (10), the results of figure 16, and the measured free-stream nuclei distribution. The calculated size distribution departs substantially from the measured distribution. The predicted bubble size range is about twice the observed size range. The number of medium sized bubbles predicted is smaller than the observed percentage. For small as well as large bubble sizes more bubbles are predicted than measured. These discrepancies may be the result of several phenomena. First, the maximum size achieved by a nucleus subjected to a specific pressure history may not be adequately predicted by the Rayleigh–Plesset equation since bubble growth may be limited by the positive pressure gradients above the headform surface. Once the bubble has grown sufficiently, the mean pressure on the bubble surface will be larger than the surface pressure used in the Rayleigh–Plesset calculation, reducing the driving force for bubble growth. Furthermore, the experimental bubble maximum size distributions often show several maxima which were repeatable for nominally fixed operating conditions. These distributions cannot be simulated with simple, smooth nuclei distributions. It seems likely that these maxima are the result of a complicated nuclei number distribution. Such detail could not be ascertained using the current holographic nuclei distribution methodology; its existence was only revealed by the electrode system which permits very large quantities of data on bubble size distributions.

7. Conclusion

Although theories of individual bubble cavitation abound, this study demonstrates that a great deal may still be learned through the observation of naturally occurring cavitation bubbles, especially bubbles formed in flows near surfaces. Cavitation bubbles are significantly affected by the viscous flow near surfaces, and this in turn effects their noise production and possibly their damage potential. Yet, numerical integration of the Rayleigh–Plesset equation provided a reasonable base for comparison with the experimentally measured data. The relationship between the nuclei flux and the resulting cavitation was successfully predicted based upon simple parameters derived from the non-cavitating flow around the body, although estimation of the bubble maximum size distribution was more difficult.

By combining the results of this study, noise of travelling bubble cavitation may be systematically synthesized. Analysis of cavitation event statistics and size distributions can relate the free-stream nuclei distribution to the cavitation process. And, once the number and size of the cavitation events are known, the total noise emission may be estimated based on the single-bubble measurements. The results presented here are useful for the case of limited cavitation, but multiple-bubble effects must be included to characterize flows in which the bubbles interact with one another. The importance of the nuclei number distribution as a parameter in cavitation studies cannot be overemphasized, although simple and accurate methods are still needed to measure this quantity with speed, ease, and precision.

The authors would like to thank Professor Allan Acosta for his advice and considerations. We would also like to acknowledge the assistance of Sanjay Kumar and Douglas Hart. This work was supported by the Office of Naval Research under contract number N-00014-85-K-0397.

REFERENCES

D'Agostino, L., Brennen, C. E. & Acosta, A. J. 1988 Linearized dynamics of two-dimensional bubbles and cavitating flows over slender surfaces. *J. Fluid Mech.* **199**, 155–176.

Arakeri, V. H. & Acosta, A. J. 1973 Viscous effects in the inception of cavitation on axisymmetric bodies. *Trans. ASME* I: *J. Fluids Engng* **95**, 519–527.

Arakeri, V. H. & Shangumanathan, V. 1985 On the evidence for the effect of bubble interference on cavitation noise. *J. Fluid Mech.* **159**, 131–150.

Baiter, H. J. 1974 Aspects of cavitation noise. In *Symp. on High Powered Propulsion of Ships, Wageningen, The Netherlands. Publication No.* 490, pp. 1–39.

Baiter, H. J. 1986 On different notions of cavitation noise and what they imply. In *Intl Symp. on Cavitation and Multiphase Flow Noise. ASME FED* vol. 45, pp. 107–118.

Barker, S. J. 1975 Measurement of radiated noise in the Caltech high-speed water tunnel – Part II: Radiated noise from cavitating hydrofoils. *Rep.* Guggenheim Aeronautics Lab., California Institute of Technology.

Benjamin, T. B. & Ellis, A. T. 1966 The collapse of cavitation bubbles and the pressures thereby produced against solid boundaries. *Phil. Trans. R. Soc. Lond.* A **260**, 221–240.

Bernier, J. N. 1981 Unsteady two-phase flow instrumentation and measurement. *Rep.* E200.4. California Institute of Technology, Division of Engineering and Applied Science.

Blake, J. R. & Gibson, D. C. 1987 Cavitation bubbles near boundaries. *Ann. Rev. Fluid Mech.* **19**, 99–123.

Blake, W. K. 1986 Mechanics of flow induced sound and vibration. In *Introduction to Bubble Dynamics and Cavitation*, Vol. 1, Chap. 6, pp. 370–425. Academic.

Blake, W. K., Wolpert, M. J. & Geib, F. E. 1977 Cavitation noise and inception as influenced by boundary layer development on a hydrofoil. *J. Fluid Mech.* **80**, 617–640.

Ceccio, S. L. 1990 Observations of the dynamics and acoustics of travelling bubble cavitation. *Rep.* E249.11. California Institute of Technology, Division of Engineering and Applied Science.

Chahine, G. L., Courbiere, P. & Garnaud. P. 1979 Correlation between noise and dynamics of cavitation bubbles. In *Sixth Conf. on Fluid Machinery, Budapest*, Vol. 1, pp. 200–209. Akademiai Kiado.

Dreyer, J. J. 1987 Free stream microbubble effects on travelling bubble cavitation inception on the Schiebe headform. *ARL/PSU Tech. Mem.* 87–205.

Ellis, A. T. 1952 Observations on cavitation bubble collapse. *Rep.* 21-12. California Institute of Technology, Hydrodynamics Lab.

Fitzpatrick, H. M. & Strasberg, M. 1956 Hydrodynamic sources of sound. In *First Symp. on Naval Hydrodynamics, Washington, DC*, pp. 241–280. National Academy Press.

Flynn, H. G. 1964 Physics of acoustic cavitation in liquids. In *Physical Acoustics: Principles and Methods*, vol. 16 (ed. W. P. Mason), pp. 57–172. Academic.

Gates, E. M. 1977 The Influence of freestream turbulence, freestream nuclei populations, and drag reducing polymer on cavitation inception on two axisymmetric bodies. *Rep.* E182-2. California Institute of Technology, Division of Engineering and Applied Science.

Gates, E. M., Billet, M. L., Katz, J., Ooi, K. K., Holl, W. & Acosta, A. J. 1979 Cavitation inception and nuclei distribution – joint ARL-CIT experiments. *Rep.* E244-1. California Institute of Technology, Division of Engineering and Applied Science.

Hamilton, M. F. 1981 Travelling bubble cavitation and resulting noise. *Tech. Mem.* TM 81–76. Applied Research Lab., Pennsylvania State University.

Hamilton, M. F., Thompson, D. E. & Billet, M. L. 1982 An experimental study of travelling bubble cavitation and noise. In *ASME Intl Symp. on Cavitation Noise*, pp. 25–33.

Harrison, M. 1952 An experimental study of single bubble cavitation noise. *J. Acoust. Soc. Am.* **28**, 776–782.

Hoyt, J. W. 1966 Wall effect on I.T.T.C. standard head shape pressure distribution. *Contribution to 11th Intl Towing Tank Conf.*

Johnson, V. E. & Hsieh, T. 1966 The influence of gas nuclei on cavitation inception. In *Proc. Sixth Symp. on Naval Hydrodynamics, Washington DC.* National Academy Press.

Katz, J. 1981 Cavitation inception in separated flows. *Rep.* E183-5. California Institute of Technology, Division of Engineering and Applied Science.

Kling, C. L. & Hammitt, F. G. 1972 A photographic study of spark induced cavitation bubble collapse. *Trans. ASME* D: *J. Basic Engng* **94**, 825–833.

Kimoto, H. 1987 An experimental evaluation of the effects of a water microjet and a shock wave by a local pressure sensor. In *Intl Symp. on Cavitation Research Facilities and Techniques, ASME FED* vol. 57, pp. 217–224.

Knapp, R. T. & Hollander, A. 1948 Laboratory investigations of the mechanisms of cavitation. *Trans. ASME*, July 1948, p. 419.

Lauterborn, W. & Bolle, H. 1975 Experimental investigation of cavitation-bubble collapse in the neighbourhood of a solid boundary. *J. Fluid Mech.* **72**, 391–399.

Lindgren, H. & Johnsson, C. A. 1966 Cavitation inception on headforms: I.T.T.C. comparative experiments. *Eleventh Intl Towing Tank Conf. Proc., Tokyo.*

Marboe, M. L., Billet, M. L. & Thompson, D. E. 1986 Some aspects of travelling bubble cavitation and noise. In *Intl Symp. on Cavitation and Multiphase Flow Noise, ASME FED* vol. 45, pp. 119–126.

Mellon, R. H. 1956 An experimental study of the collapse of a spherical cavity in water. *J. Acoust. Soc. Am.* **28**, 447–454.

Meulen, J. H. J. van der 1980 Boundary layer and cavitation studies of NACA 16–012 and NACA 4412 hydrofoils. *Thirteen Symp. on Naval Hydrodynamics, Tokyo*, pp. 195–217. National Academy Press.

Meulen, J. H. J. van der & Renesse, R. L. van 1989 The collapse of bubbles in a flow near a boundary. *Seventeenth Symp. on Naval Hydrodynamics, The Hague*, pp. 379–392. National Academy Press.

Meyer, R. S., Billet, M. L. & Holl, J. W. 1989 Free stream nuclei and cavitation. In *Intl Symp. on Cavitation Inception, ASME FeD* vol. 89, pp. 55–62.

Morch, K. A. 1982 Energy consideration on the collapse of cavity clusters. *Appl. Sci. Res.* **38**, 313.

Morozov, V. P. 1969 Cavitation noise as a train of sound pulses generated at random times. *Sov. Phys. – Acoust.* **14**, 361–365.

Ooi, K. K. 1981 Scale effects on cavitation inception in submerged jets. *Rep.* E183-6. California Institute of Technology, Division of Engineering and Applied Science.

PARKIN, B. R. 1952 Scale effects in cavitating flow. Ph.D. thesis, California Institute of Technology.

PLESSET, M. S. & CHAPMAN, R. B. 1970 Collapse of an initially spherical vapor cavity in the neighbourhood of a solid boundary. *Rep.* 85-49. California Institute of Technology, Division of Engineering and Applied Science.

RAYLEIGH, LORD 1917 On the pressure developed in a liquid during the collapse of a spherical cavity. *Phil. Mag.* **34**, 94–98.

ROOD, E. P. 1989 Mechanisms of cavitation inception. *Intl Symp. on Cavitation Inception, ASME FED* vol. 89, pp. 1–22.

SCHIEBE, F. R. 1972 Measurement of the cavitation susceptibility of water using standard bodies. *Rep.* 118. St Anthony Falls Hydraulic Laboratory, University of Minnesota.

VOGEL, A., LAUTERBORN, W. & TIMM, R. 1989 Optical and acoustic investigations of the dynamics of laser-produced cavitation bubbles near a solid boundary. *J. Fluid Mech.* **206**, 299–338.